Structures and Physical Properties of $n = 3$ Ruddlesden–Popper Compounds $Ca_4Mn_{3-x}Nb_xO_{10}$ ($0 \leq x \leq 0.2$)

Ping Chai, Xiaojuan Liu, Minfeng Lu, Zhongli Wang, and Jian Meng*

State Key Laboratory of Rare Earth Resources Application, Changchun Institute of Applied Chemistry, and Graduate School of the Chinese Academy of Sciences, Chinese Academy of Sciences, Changchun 130022, People's Republic of China

Received June 27, 2007. Revised Manuscript Received December 11, 2007

The Ruddlesden–Popper series of compounds $Ca_4Mn_{3-x}Nb_xO_{10}$ ($x = 0$–0.2) have been prepared by solid-state methods. Structural, magnetic, electrical, and magnetoresistive studies were performed on the compounds. Nb doping caused increases in both unit cell volume and octahedral distortion. The magnetization measurements indicated that the doped samples displayed ferromagnetism-like behavior, which could be explained by the double-exchange interaction between Mn^{4+} and Mn^{3+} induced by the charge-compensation effect. A phase-separation picture with the appearance of ferromagnetic clusters embedded in an antiferromagnetic matrix described the magnetic ground state of the doped samples well. All of the samples exhibited semiconducting behavior over the whole measured temperature range, with the high-temperature behavior better described by the small polaron conduction model and the low-temperature behavior by the two-dimensional version of Mott's variable range hopping model. A large magnetoresistance effect was observed for all of the doped samples, and its value rose with decreasing temperature and increasing Nb content, attaining 51% at 40 K under a magnetic field of 5 T for the $x = 0.2$ sample. Calculated results for $Ca_4Mn_3O_{10}$ and $Ca_4Mn_{2.8}Nb_{0.2}O_{10}$ samples further verified the corresponding experimental determinations.

Introduction

The doped perovskite manganites $R_{1-x}A_xMnO_3$ (R = rare-earth ion; A = divalent alkaline metal) were the subject of numerous studies in terms of both basic research and potential technological applications in magnetic memory devices, since the colossal magnetoresistance (CMR) effect was discovered in these systems.[1] As a result of complicated competition of several interactions, including ferromagnetic double exchange, antiferromagnetic superexchange, charge ordering, and the Jahn–Teller effect of the Mn^{3+} ion, these compounds have a strong tendency toward phase separation,[2] which is widely considered to be the origin of the CMR effect.[3]

It is well-known that three-dimensional (3D) perovskite manganites belong to the $n = \infty$ case of the Ruddlesden–Popper (RP) phase with general formula $(RA)_{n+1}Mn_nO_{3n+1}$.[4] Layered RP phases, which have structures consisting of alternate stacking of n perovskite block layers and a rock-salt-type layer, exhibit a complex evolution of magnetic and electronic properties as a function of composition; these properties generally resemble those of the corresponding 3D perovskite manganites but simultaneously have their own specialty. The most notable manifestation of their specialty is that single-crystal $La_{1.2}Sr_{1.8}Mn_2O_7$ shows an extremely large MR of 20 000%, which is much greater than that of the 3D perovskite manganites.[5] It has been found that the specialty of layered RP phases originates from the dimensionality effect. The introduction of the rock-salt layer in the layered RP phase weakens the exchange interactions between interlayers of MnO_2, thus inducing an anisotropic decrease in the 3d bandwidth, and finally influences the physical properties of these systems to an extent that is related to the value of n.[6] Therefore, in view of the novel properties of the electron-doped $CaMnO_3$ system,[7–12] a few studies focusing on the electron-doped RP phase have been conducted in order to obtain some new observations different from those for the 3D perovskite manganites. In particular, electron-doped $Ca_4Mn_3O_{10}$ systems are of considerable interest. For the $Ca_{4-x}La_xMn_3O_{10}$ system,[13] although a CMR effect was observed, the structural phase transition involving changes in x, which had been found in $Ca_{1-x}La_xMnO_3$,[9] disappeared. For the $Ca_4Mn_{3-x}V_xO_{10}$ system,[14] ferromagnetic behavior and a CMR effect were also found, but the

* Corresponding author. E-mail: jmeng@ciac.jl.cn.

(1) Jin, S.; Tiefel, T. H.; McCormack, M.; Fastnacht, R. A.; Ramesh, R.; Chen, L. H. *Science* **1994**, *264*, 413.
(2) Moreo, A.; Yunoki, S.; Dagotto, E. *Science* **1999**, *283*, 2034.
(3) Dagotto, E.; Hotta, T.; Moreo, A. *Phys. Rep.* **2001**, *344*, 1.
(4) Ruddlesden, S. N.; Popper, P. *Acta Crystallogr.* **1958**, *11*, 541.
(5) Moritomo, Y.; Asamitsu, A.; Kuwahara, H.; Tokura, Y. *Nature* **1996**, *380*, 141.
(6) Lago, J.; Battle, P. D.; Rosseinsky, M. J. *J. Phys.: Condens. Matter* **2000**, *12*, 2505.
(7) Zeng, Z.; Greenblatt, M.; Croft, M. *Phys. Rev. B* **1999**, *59*, 8784.
(8) Neumeier, J. J.; Cohn, J. L. *Phys. Rev. B* **2000**, *61*, 14319.
(9) Ling, C. D.; Granado, E.; Neumeier, J. J.; Lynn, J. W.; Argyriou, D. N. *Phys. Rev. B* **2003**, *68*, 134439.
(10) Mahendiran, R.; Maignan, A.; Martin, C.; Hervieu, M.; Raveau, B. *Phys. Rev. B* **2000**, *62*, 11644.
(11) Martin, C.; Maignan, A.; Hervieu, M.; Raveau, B. *Phys. Rev. B* **2000**, *63*, 100406.
(12) Shames, A. I.; Rozenberg, E.; Martin, C.; Maignan, A.; Raveau, B.; André, G.; Gorodetsky, G. *Phys. Rev. B* **2004**, *70*, 134433.
(13) Witte, N. S.; Goodman, P.; Lincoln, F. J.; March, R. H.; Kennedy, S. J. *Appl. Phys. Lett.* **1998**, *72*, 853.

10.1021/cm071712s CCC: $40.75
Published on Web 01/19/2008

anomalous diamagnetism appearing in $CaMn_{1-x}V_xO_3$ systems[15] was completely suppressed. Similarly, the $Ca_4Mn_{3-x}Mo_xO_{10}$ system[16] displayed both an inhomogeneous magnetic ground state with ferromagnetic (FM) clusters embedded in an antiferromagnetic (AFM) matrix and a CMR effect, but the charge order and orbital order observed in $CaMn_{1-x}Mo_xO_3$ systems[11] were not found. It seems that the layered electron-doped systems tend to exhibit suppression of some of the properties present in the corresponding 3D systems. Further studies concerning electron doping by other ions need to be done in order to confirm this point of view, which is reminiscent of the Nb-doped $CaMnO_3$ system. Raveau et al.[17] first investigated the $CaMn_{1-x}Nb_xO_3$ system and found ferromagnetism-like behavior and a large MR effect. Later, Gou et al.[18] studied the same system but found magnetic and transport properties that differed from those reported by Raveau et al. This situation implies that the doping effect induced by Nb is very interesting. However, no studies concerning Nb doping in the $Ca_4Mn_3O_{10}$ system have been reported to date.

In view of the above discussion, we performed the substitution of Mn by Nb in the $n = 3$ RP phase $Ca_4Mn_3O_{10}$ in order to obtain complete insight into this system, with the further expectation of providing an understanding of the effect of dimensionality on the physical properties of such samples. In this paper, we report on detailed studies of the structural, magnetic, and transport properties of $Ca_4Mn_{3-x}Nb_xO_{10}$ ($0 \leq x \leq 0.2$).

Experimental Section

Polycrystalline samples of $Ca_4Mn_{3-x}Nb_xO_{10}$ ($x = 0$, 0.05, 0.1, and 0.2) were synthesized from high-purity powders of $CaCO_3$, Mn_2O_3, and Nb_2O_5 using standard solid-state techniques in air. $CaCO_3$ was used as received, and the powders of Mn_2O_3 and Nb_2O_5 were dehydrated at 900 °C for 12 h prior to use. Stoichiometric quantities of powders were weighed, mixed, ground thoroughly in an agate mortar, and calcined in alumina crucibles at 800 °C for 24 h. The resulting powders were then ground, pelletized, and sintered at 1020 °C for 30 h and at 1220 °C for 60 h with intermediate grinding. Finally, the products were reground, pressed into pellets, and heated at 1320 °C for 24 h with subsequent cooling to room temperature in the furnace.

The phase purities and crystal structures of the samples were examined by X-ray powder diffraction (XRD) at room temperature (RT) on a Rigaku D/Max 2500 powder diffractometer (Cu Kα radiation, $\lambda = 1.5406$ Å). The XRD patterns were obtained between 5° and 120° in steps of 0.02° with a counting time of 2 s per step and analyzed by Rietveld refinements using the GSAS programs.[19] The background was modeled using a shifted Chebyschev polynomial function, and a pseudo-Voigt function was used to fit the peak shapes in all cases. The initial positional parameters were obtained from the data previously reported for $Ca_4Mn_3O_{10}$.[20] An overall isotropic temperature factor for each sample was refined. The occupation factors were fixed by taking sample stoichiometry into account, assuming that the Nb cations were randomly distributed over the two Mn sites and that all of the oxygen sites were fully occupied. A preferred orientation correction and an absorption correction were included in the refinement. In the final run, the following parameters were refined: scale factor, background coefficients, unit cell parameters, pseudo-Voigt and asymmetry parameters for the peak shape, positional coordinates, and isotropic thermal factor.

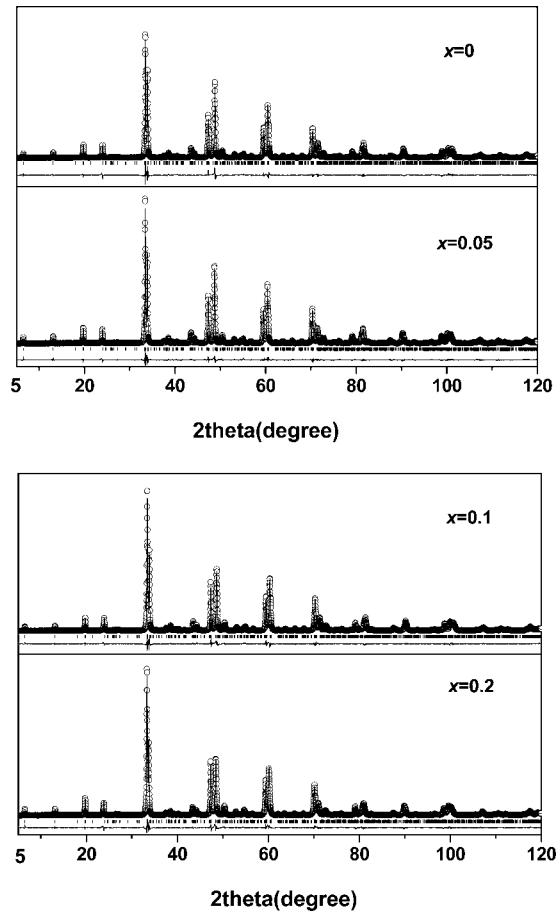

Figure 1. Observed (circles) and calculated (solid lines) Rietveld refinement plots of the XRD patterns of the $Ca_4Mn_{3-x}Nb_xO_{10}$ phases. The difference between the observed and calculated plots is shown at the bottom of each pattern. Vertical tick marks represent allowed reflections.

Elemental analysis using the energy-dispersive X-ray (EDX) emission technique gave the stoichiometric composition within experimental errors. X-ray photoelectron spectroscopy (XPS) measurements were performed using an ESCALAB MKII spectrometer with an Al Kα X-ray excitation source.

Measurements of magnetization as a function of temperature under zero-field-cooling (ZFC) and field-cooling (FC) as well as of magnetization as a function of the applied magnetic field ($M-T$ and $M-H$ measurements, respectively) were performed on a Quantum Design superconducting quantum interference device (SQUID)-based Magnetic Properties Measurement System. Transport properties were measured with a standard four-probe technique using a Quantum Design Physical Property Measurement System.

(14) Carvalho, M. D.; Borges, R. P.; Girão, A. V.; Cruz, M. M.; Melo Jorge, M. E.; Bonfait, G.; Dluzewski, P.; Godinho, M. *Chem. Mater.* **2005**, *17*, 4852.
(15) Ang, R.; Sun, Y. P.; Ma, Y. Q.; Zhao, B. C.; Zhu, X. B.; Song, W. H. *J. Appl. Phys.* **2007**, *100*, 063902.
(16) Lu, W. J.; Sun, Y. P.; Ang, R.; Zhu, X. B.; Song, W. H. *Phys. Rev. B* **2007**, *75*, 014414.
(17) Raveau, B.; Zhao, Y. M.; Martin, C.; Hervieu, M.; Maignan, A. *J. Solid State Chem.* **2000**, *149*, 203.
(18) Guo, Y. Q.; Li, W. *Chem. Mater.* **2005**, *17*, 2735.
(19) Larson, A. C.; von Dreele, R. B. *General Structure Analysis System (GSAS)*; Report LAUR 86–748; Los Alamos National Laboratory: Los Alamos, NM, 1990.
(20) Battle, P. D.; Green, M. A.; Lago, J.; Millburn, J. E.; Rosseinsky, M. J.; Vente, J. F. *Chem. Mater.* **1998**, *10*, 658.

Table 1. Refined Values of Unit Cell Parameters and Volumes, Selected Mn−O Bond Lengths (Å) and Mn−O−Mn Angles (deg), and Reliability Factors for $Ca_4Mn_{3-x}Nb_xO_{10}$ ($x = 0$, 0.05, 0.1, and 0.2), Space Group *Pbca*, from RT XRD

	$x = 0$	$x = 0.05$	$x = 0.1$	$x = 0.2$
a (Å)	5.26497(11)	5.27616(15)	5.28532(18)	5.30657(25)
b (Å)	5.26136(12)	5.27203(14)	5.28054(18)	5.30009(25)
c (Å)	26.8171(3)	26.8189(4)	26.8169(4)	26.8183(4)
V (Å^3)	742.858(13)	745.998(26)	748.444(28)	754.271(19)
$10^4 \times s^a$	3.43	3.92	4.52	6.11
Mn(1)−O(1) × 2	1.901(8)	1.904(6)	1.916(7)	1.919(7)
Mn(1)−O(5) × 2	1.91(2)	1.93(2)	1.94(2)	1.98(2)
Mn(1)−O(5) × 2	1.88(2)	1.88(2)	1.88(2)	1.90(2)
⟨Mn(1)−O⟩	1.90(2)	1.90(2)	1.91(2)	1.93(2)
$10^5 \times \Delta_d[Mn(1)O_6]^b$	4.63	12.15	16.78	31.51
Mn(2)−O(1)	1.923(8)	1.931(7)	1.936(7)	1.942(8)
Mn(2)−O(2)	1.914(7)	1.894(6)	1.919(6)	1.909(8)
Mn(2)−O(3)	1.91(2)	1.93(2)	1.92(2)	1.95(2)
Mn(2)−O(3)	1.88(2)	1.90(2)	1.93(2)	1.92(2)
Mn(2)−O(4)	1.92(2)	1.93(1)	1.90(2)	1.94(2)
Mn(2)−O(4)	1.87(2)	1.86(2)	1.85(2)	1.82(2)
⟨Mn(2)−O⟩	1.90(2)	1.91(1)	1.91(2)	1.91(2)
$10^5 \times \Delta_d[Mn(2)O_6]^b$	11.66	18.72	22.65	53.57
⟨Mn−O⟩	1.90(2)	1.90(1)	1.91(2)	1.92(2)
O(1)−Mn(1)−O(1)	180.0(0)	179.98(0)	179.972(0)	179.98(0)
O(1)−Mn(2)−O(2)	175.4(6)	168.6(6)	177.4(7)	176.6(8)
Mn(1)−O(1)−Mn(2)	162.4(6)	158.5(5)	160.6(6)	158.0(6)
Mn(1)−O(5)−Mn(1)	154.7(6)	157.6(5)	159.7(7)	156.8(7)
Mn(2)−O(3)−Mn(2)	162.7(9)	156.1(6)	162.9(7)	159.3(7)
Mn(2)−O(4)−Mn(2)	158.5(8)	161.2(6)	155.1(5)	164.0(8)
χ^2	1.372	2.40	2.434	2.530
R_p (%)	8.11	7.31	7.41	7.30
R_{wp} (%)	10.55	9.82	9.85	9.79

[a] s is the spontaneous orthorhombic strain, defined as $s = 2(a - b)/(a + b)$. [b] Δ_d is a parameter indicating the relative distortion of the MnO_6 octahedra, defined as $\Delta_d = \sum_{n=1}^{6}[(d_n - \langle d\rangle)/\langle d\rangle]^2/6$, where d_n is a Mn−O distance.

Calculations were performed using the full-potential augmented plane waves plus local orbital method. The experimentally refined crystal structures for $Ca_4Mn_3O_{10}$ and $Ca_4Mn_{2.8}Nb_{0.2}O_{10}$ were used. The muffin-tin sphere radii were chosen to be 2.02, 1.78, 1.82, and 1.58 b for Ca, Mn, Nb, and O atoms, respectively, with $RK_{max} = 7.0$. The Perdew−Burke−Ernzerhof standard generalized gradient approximation (GGA) was adopted for the exchange-correlation potential.[21] Electronic structures were calculated with antiferromagnetic configurations. Self-consistent calculations were considered to be converged when the energy convergence was less than 10^{-5} Ry.

Results and Discussion

The XRD patterns demonstrated that each composition of $Ca_4Mn_{3-x}Nb_xO_{10}$ ($x = 0$, 0.05, 0.1, and 0.2) was single-phase with a distorted layered perovskite-type structure. For all of the samples, the observed peaks were refined on the basis of an orthorhombic structure with space group *Pbca*. The XRD diagrams, including the raw data, the global fitted profile, and the difference, for all of the members of $Ca_4Mn_{3-x}Nb_xO_{10}$ are shown in Figure 1. Values of the final lattice parameters, unit cell volumes, reliability factors, and selected bond lengths and angles for each of the samples are listed in Table 1. The crystal structure of $Ca_4Mn_3O_{10}$ is shown in Figure 2.

It is clear that the unit cell volume increased with increasing Nb content, as seen in Figure 3. This phenomenon can be explained by the increase in the average ionic size at the Mn position due to successful substitution of Mn by Nb. On one hand, since the radius of Nb^{5+} (0.64 Å) is larger than that of Mn^{4+} (0.53 Å), the substitution of Mn^{4+} by Nb^{5+} can lead to an increase in the average ionic radius at the Mn site and thus induce the lattice expansion. On the other hand, the Nb^{5+} substitution should lead to some reduction of Mn^{4+} to Mn^{3+} (whose radius is 0.645 Å), which can also cause an increase in the unit cell volume. As far as the unit cell parameters are concerned, it is obvious that the

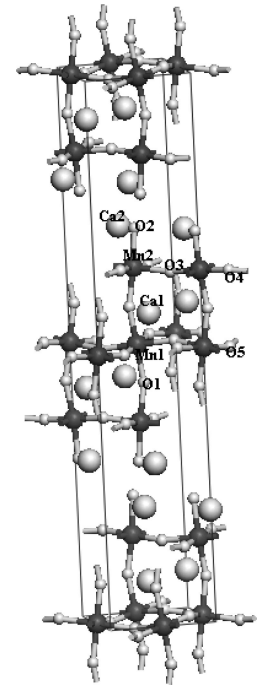

Figure 2. Schematic crystal structure of $Ca_4Mn_3O_{10}$. Large, medium, and small spheres represent Ca, Mn, and O, respectively.

(21) Perdew, J. P.; Burke, K.; Ernzerhof, M. *Phys. Rev. Lett.* **1996**, *77*, 3865.

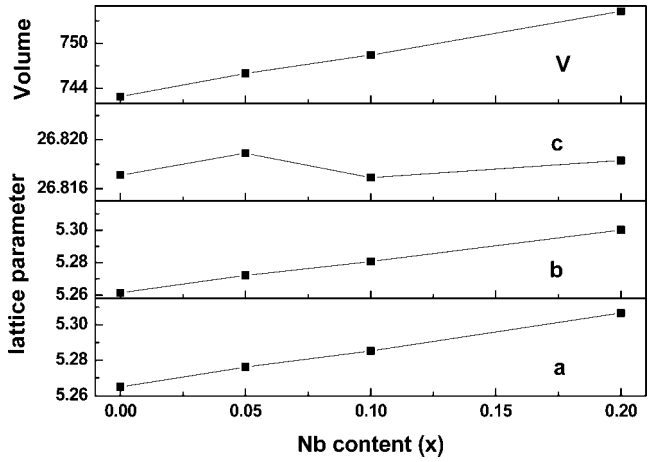

Figure 3. Lattice parameters and unit cell volume as a function of Nb content.

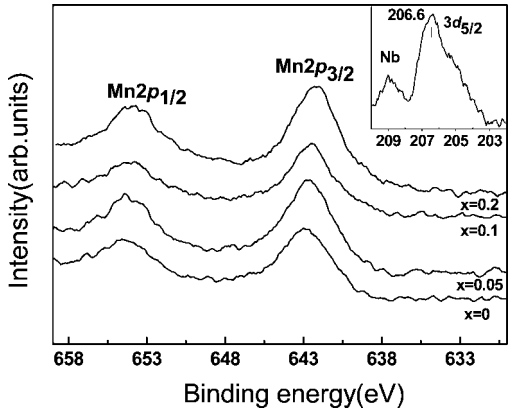

Figure 4. XPS spectra of the Mn 2p region for $Ca_4Mn_{3-x}Nb_xO_{10}$. The inset shows the XPS spectrum of the Nb 3d region for the $x = 0.2$ compound.

a and *b* parameters both displayed gradual enlargement while the *c* parameter showed very little variation with increasing Nb content, as shown in Figure 3. Furthermore, the spontaneous orthorhombic strain, defined as $s = 2(a - b)/(a + b)$, progressively increased, as indicated in Table 1. Considering that the *s* parameter is a measure of the distortion of the octahedron,[22] we can conclude that the octahedral distortion increased with increasing Nb content, consistent with an increase in the Mn^{3+} Jahn–Teller effect. In order to further confirm the valence states of the Mn and Nb ions, we performed XPS measurements on the Mn 2p and Nb 3d regions. Figure 4 shows the XPS spectra of the Mn 2p region for each of the samples. For the $x = 0$ sample, as expected, the centered value of the Mn $2p_{3/2}$ peak appeared at 642.8 eV, in agreement with literature data of MnO_2[23] and corresponding to Mn^{4+}. As the amount of Nb increased, the Mn $2p_{3/2}$ peak shifted slightly toward lower binding energy and reached 642.1 eV for the $x = 0.2$ sample; this result, together with the fact that the binding energy of Mn^{3+} in Mn_2O_3 is 641.5 eV,[24] indicated the coexistence of Mn^{3+} and Mn^{4+} in the doped samples. The binding energy of Nb $3d_{5/2}$ for the $x = 0.2$ sample (shown in the inset) was 206.6 eV, which was consistent with that of the Nb_2O_5,[25] indicating that the Nb ion remained pentavalent. This result was also compatible with the fact that the Nb^{5+} is most stable in the air. In summary, the XPS measurements provided additional evidence that Nb entered into the lattice. Since oxygen vacancies have a vital influence on the lattice parameters and physical properties of this series of compounds, efforts to indirectly determine the oxygen content of the $Ca_4Mn_{3-x}Nb_xO_{10}$ samples were attempted but failed because of sample dissolution problems (iodometric titration) and enhanced chemical stability toward reduction (thermogravimetric analysis). Other publications employing an analogous synthesis method reported almost stoichiometric oxygen content for $Ca_4Mn_3O_{10}$.[20,26] Therefore, on the basis of the regular variation of the lattice parameters, we conclude that oxygen vacancies were negligible in our samples.

The partial list of refined bond lengths and angles in Table 1 also contains valuable crystal structure information. It can be seen that the average Mn−O bond length ($\langle$Mn−O$\rangle$) increased with the extent of Nb doping. In addition, both the divergence between the Mn(1)−O(1) and Mn(1)−O(5) bond lengths and that between the Mn(2)−O(*k*) ($k = 1-4$) bond lengths were enhanced with increasing Nb content. In order to quantify the relative distortion of the MnO_6 octahedra, we employed the parameter Δ_d, defined as $\Delta_d = \sum_{n=1}^{6}[(d_n - \langle d\rangle)/\langle d\rangle]^2/6$, where d_n is a Mn−O bond length; the value of this parameter increases when the deviation of the Mn−O bond length is enhanced compared with the average Mn−O value.[22] Obviously, both the $\Delta_d(1)$ and $\Delta_d(2)$ values showed significant increases as *x* increased, indicating enhancement of the distortion of the $Mn(1)O_6$ and $Mn(2)O_6$ octahedra. This result was compatible with an increase in the amount of Mn^{3+}, which can lead to Jahn−Teller distortion of the octahedra. Furthermore, it is clear that $\Delta_d(1)$ was smaller than $\Delta_d(2)$ and that the axial O−Mn(1)−O bond angle was closer to 180° than the axial O−Mn(2)−O bond angle for each sample, demonstrating that the $Mn(1)O_6$ octahedra were more regular than the $Mn(2)O_6$ octahedra for all of the samples, in consonance with the previous report on $Ca_4Mn_3O_{10}$.[20,27]

Figure 5a presents the temperature dependence of the ZFC and FC magnetizations for each of the samples. It is obvious that the $Ca_4Mn_{3-x}Nb_xO_{10}$ samples exhibited a complicated inhomogeneous magnetic phase. For the $x = 0$ sample, the ZFC curve exhibited a cusp at 115 K, from which the FC curve simultaneously showed a remarkable increase with decreasing temperature. This behavior was in good agreement with previous reports[6,14,16] and suggested a spin-canted AFM behavior at low temperature that has been effectively explained by a Dzyaloshinskii−Moriya term introduced by the orthorhombic distortion of the crystal structure. The ZFC curve also showed an unexpected increase at 60 K, which was not reported in the previous literature.[6,14,16] This could

(22) Alonso, J. A.; Martínez-Lope, M. J.; Casais, M. T. *Inorg. Chem.* **2000**, *39*, 917.
(23) Ansell, R. O.; Dickinson, T.; Povey, A. F. *Corros. Sci.* **1978**, *18*, 245.
(24) Ivanov-Emin, B. N.; Nevskaya, N. A.; Zaitsev, B. E.; Ivanova, T. M. *Zh. Neorg. Khim.* **1982**, *27*, 3101.
(25) Garbassi, F.; Bart, J. C. J.; Petrini, G. *J. Electron Spectrosc. Relat. Phenom.* **1981**, *22*, 95.
(26) Fisher, B.; Patlagan, L.; Reisner, G. M.; Knizhnik, A. *Phys. Rev. B* **2000**, *61*, 470.
(27) Fawcett, I. D.; Sunstrom, J. E.; Greenblatt, M.; Croft, M.; Ramanujachary, K. V. *Chem. Mater.* **1998**, *10*, 3643.

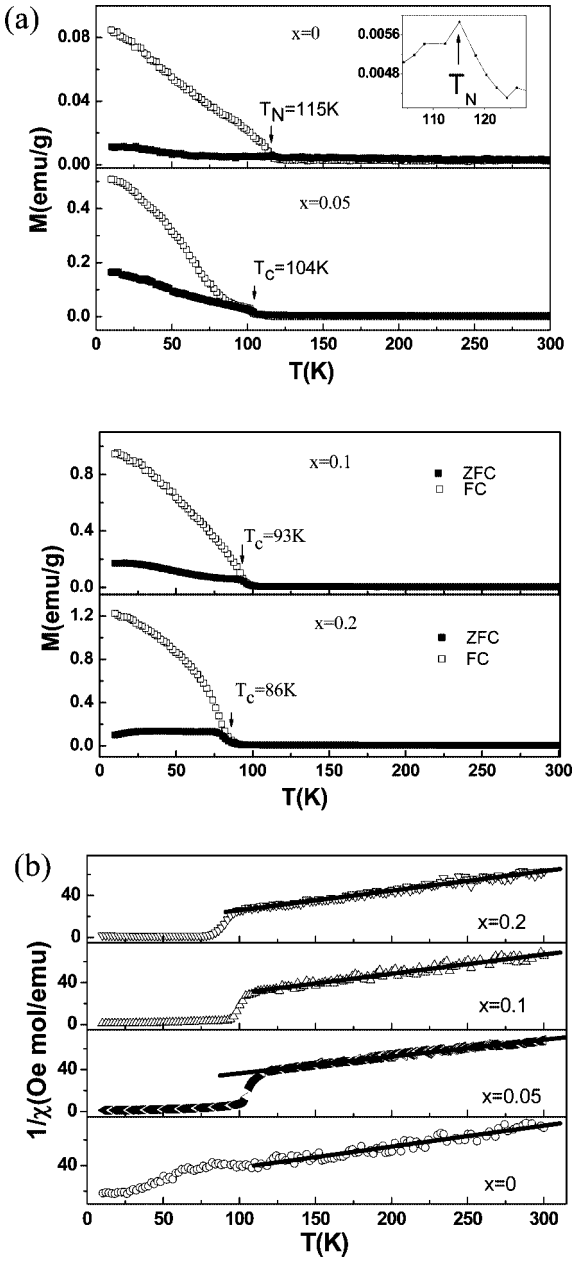

Figure 5. (a) Magnetization as a function of temperature measured under a field strength of 100 Oe for $Ca_4Mn_{3-x}Nb_xO_{10}$ (FC curves, open symbols; ZFC curves, solid symbols). The inset shows the enlarged ZFC curve around 115 K for $x = 0$. (b) Inverse ZFC curves (symbols) with Curie–Weiss fits (solid lines).

be ascribed to the existence of a small amount of an impurity in the samples that was undetected by XRD and yielded an additional Curie transition at 60 K. Another possible explanation is connected with depinning of magnetic domain walls at a particular temperature and magnetic field, where the pinning was due to some inhomogeneity or defects at the walls.[28] Isothermal hysteresis loops at 5 K for this sample (Figure 6) showed a small ferromagnetic component, as expected; however, this component was larger than that reported previously, where M increased almost linearly with H, suggesting that the existence of an impurity phase was the more probable explanation.

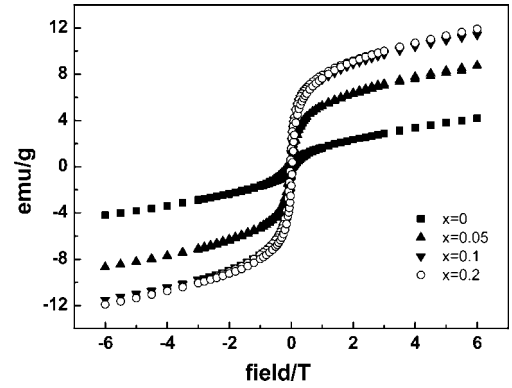

Figure 6. Direct-current magnetization as a function of magnetic field measured at 5 K for $Ca_4Mn_{3-x}Nb_xO_{10}$.

Table 2. Effective Magnetic Moments (μ_{exp}) and Weiss Temperatures (θ_p) Obtained from Fits to the Curie–Weiss Law, Calculated Effective Magnetic Moments (μ_{calc}), and Activation Energies (E_ρ) and Characteristic Temperatures (T_0) Obtained by SPC and VRH Fitting, Respectively

x	μ_{exp} (μ_B)	μ_{calc} (μ_B)	θ_P (K)	E_ρ (meV)	T_0 (K)
0	4.08	3.87	−137	84.3	3.5×10^5
0.05	4.12	3.89	−128	74.7	2.4×10^5
0.1	3.87	3.91	−63	71.4	2.7×10^5
0.2	3.92	3.94	−39	74.8	5.9×10^5

With regard to the substituted samples, the ZFC and FC curves both showed a sharp increase below T_C, and a magnetization magnitude significantly larger than that of $Ca_4Mn_3O_{10}$ was observed. These results indicated a ferromagnetism-like behavior, which can be explained by the fact that the high-valence Nb ions induced the presence of Mn^{3+} species in the samples. As a result, the double-exchange (DE) interaction between Mn^{4+} and Mn^{3+} could be established, justifying the observed ferromagnetic component. The magnetic moment increased with increasing Nb content, and the increased magnitude gradually diminished. The T_C value showed a gradual decrease as x increased. These results can be attributed to the combined interaction of many effects. First, with the increase in doping content, the concentration of Mn^{3+} carriers in the Mn^{4+} matrix increased, enhancing the ferromagnetism via the DE interaction at the expense of the $Mn^{4+}-O-Mn^{4+}$ antiferromagnetic interaction. On the other hand, the Mn^{3+} Jahn–Teller effect could cause local lattice distortion that would tend to trap the electrons and thus suppress the DE ferromagnetic interaction.[29] Additionally, introduction of the nonmagnetic Nb ion not only diluted the magnetic Mn ion but also enlarged the separation between the Mn ions. Both of these factors could lead to the reduction of magnetization. As a consequence, the competition among these three effects resulted in a nonlinear variation in both magnetic moment and Curie temperature with Nb content. There was a big divergence between the ZFC and FC curves at low temperature for the doped samples, which implies that these samples contained either inhomogeneous clusters or a homogeneous spin-glass state. It is reasonable to think that the inhomogeneous clusters were present, because the small amount of doping would cause the Mn^{3+} to be sparsely distributed in the Mn^{4+} matrix, leading to the formation of

(28) Duan, P.; Chen, Z. H.; Dai, S. Y.; Zhou, Y. L.; Lu, H. B.; Jin, K. J.; Cheng, B. L. *Appl. Phys. Lett.* **2004**, *84*, 4741.

(29) Millis, A. J. *Nature* **1998**, *392*, 147.

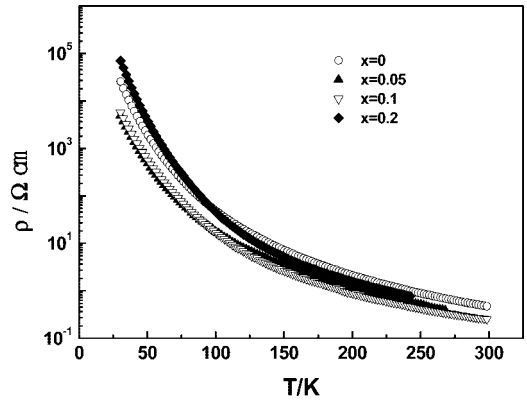

Figure 7. Zero-field resistivity as a function of temperature for $Ca_4Mn_{3-x}Nb_xO_{10}$.

local ferromagnetic clusters embedded in the antiferromagnetic matrix. It has been reported that the slightly doped $La_xSr_{4-x}Mn_3O_{10}$, $La_xCa_{4-x}Mn_3O_{10}$, and $Ca_4Mn_{3-x}Mo_xO_{10}$ systems also exhibit FM clusters in their ground states at low temperature.[16,30,31]

The inverse susceptibilities are plotted versus temperature for each of the samples in Figure 5b. The paramagnetic regions at high temperature were well-fitted by the Curie–Weiss law, as indicated by the solid lines in the figure. The Weiss temperatures and effective magnetic moments obtained from the fitting procedure are listed in Table 2. It can be seen that all of the θ values were negative, demonstrating that all of the samples remained antiferromagnetic. Meanwhile, the absolute value of θ decreased as the Nb content increased, implying that the AFM interaction decreased with Nb substitution. All of these results further confirmed that short-range ferromagnetic clusters rather than long-range ferromagnetic ordering appeared in the system and that the number of FM clusters rose with the extent of Nb doping. It should be noticed that the θ value for the $x = 0$ sample was -137 K, which was significantly different from the value of approximately -500 K reported previously. This large discrepancy can be ascribed to the existence of the impurity mentioned earlier, whose Curie transition at 60 K caused the value of θ to be smaller. An analogous phenomenon has been reported in other manganites, where the existence of impurities was regarded as the primary explanation.[32] In addition, the observed effective magnetic moments were very close to the values calculated on the basis of the expected mixed valence of Mn, providing further evidence of the effective substitution of Mn by Nb in this series.

In order to further verify the magnetic properties of the samples, we measured isothermal hysteresis loops at 5 K, as shown in Figure 6. Obviously, the magnetization of each of the doped samples showed a sharp rise at low magnetic field and then a linear increase with increasing field, suggesting the existence of an inhomogeneous magnetic state consisting of FM and AFM phases. It can also been observed

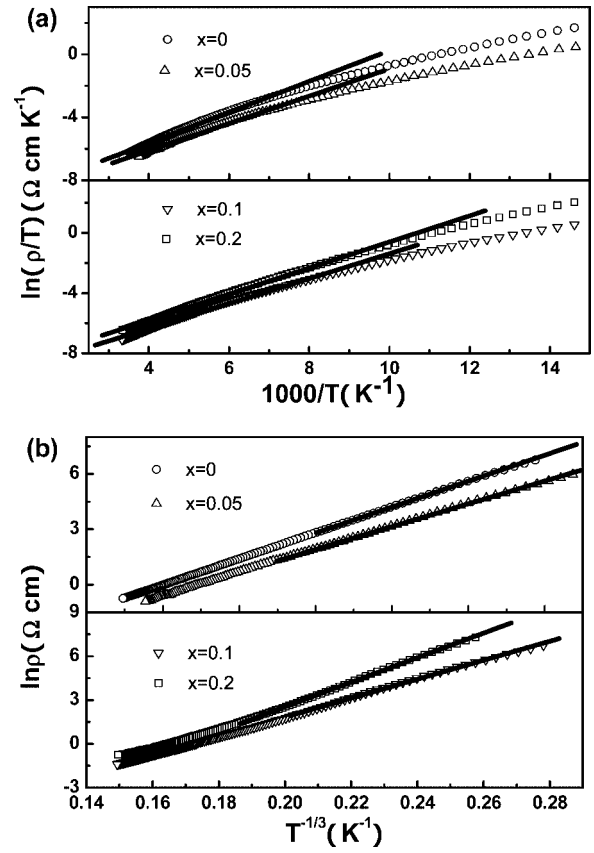

Figure 8. Plots of (a) $\ln(\rho/T)$ versus $1000/T$ in the high-temperature region fitted by the SPC model and (b) $\ln \rho$ versus $T^{-1/3}$ in the low-temperature region fitted by the VRH model for $Ca_4Mn_{3-x}Nb_xO_{10}$ at zero magnetic field. Symbols represent data points, and the fits are shown as solid lines.

that the magnetization did not saturate even in the applied field of 6 T and that hysteresis appeared only at lower fields for all of the samples. In view of the fact that hysteresis appears even at high field for spin glass, it is logical to conclude that Nb doping led to the occurrence of FM clusters rather than a spin-glass state.

The temperature dependence of the resistivity of $Ca_4Mn_{3-x}Nb_xO_{10}$ is displayed in Figure 7. All of the samples displayed semiconducting behavior over the entire measured temperature range. At the same time, as the Nb content increased, the resistivity first decreased and then increased, mainly as a consequence of the competition between two factors, one favoring a decrease in resistivity and the other favoring an increase. The former originates from an increase in the number of itinerant electrons due to the enlargement of the content of the FM clusters with Nb doping. The latter originates from a reduction of the itinerancy of these electrons due to the increased number of Mn^{3+} Jahn–Teller ions and to the introduction of the nonmagnetic Nb^{5+} ions. Obviously, the former dominated for the $x = 0.05$ and $x = 0.1$ samples, but the latter prevailed for $x = 0.2$. Moreover, no anomalous feature appeared around the magnetic transition temperature, demonstrating that for all of the samples, the content of the FM clusters was too small to reach the percolation threshold. It should be noted that the magnitude of the variation of the resistivity was not significant with increasing Nb content. Small changes in the magnitude of the resistivity at high temperature have also been reported in the $La_{5/8-x}Pr_xCa_{3/8}$-

(30) Yao, L. D.; Yang, H.; Zhang, W.; Li, F. Y.; Jin, C. Q.; Yu, R. C. *J. Appl. Phys.* **2006**, *100*, 023907.
(31) Tang, Y. K.; Ma, X.; Kou, Z. Q.; Sun, Y.; Di, N. L.; Cheng, Z. H.; Li, Q. A. *Phys. Rev. B* **2005**, *72*, 132403.
(32) Katsufuji, T.; Mori, S.; Masaki, M.; Moritomo, Y.; Yamamoto, N.; Takagi, H. *Phys. Rev. B* **2001**, *64*, 104419.

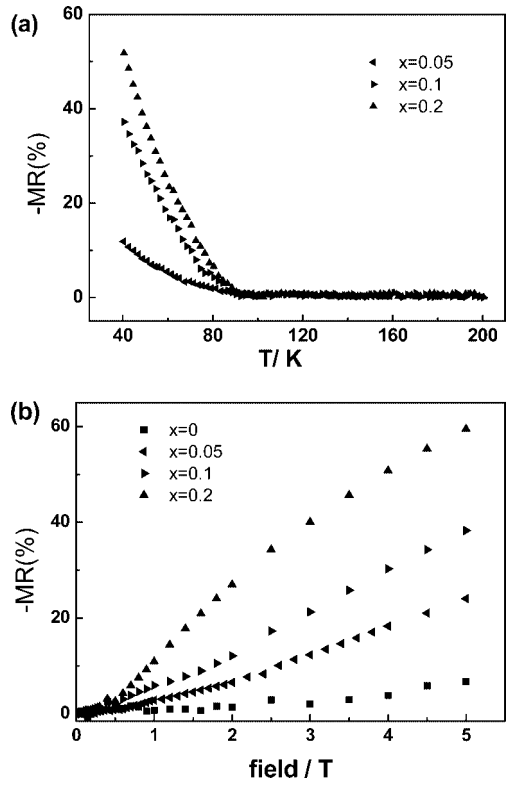

Figure 9. (a) Temperature dependence of the negative of the magnetoresistance under an applied magnetic field of 5 T. (b) Negative of the magnetoresistance as a function of magnetic field at 35 K.

MnO_3 system. In that case, this effect was ascribed to the uncertainty in the determination of the geometrical factor of the samples and regarded as an indication that the nature of the charge-carrier transport was the same for all of the samples;[33] this was probably also applicable to our samples. In addition, if one disregards the abnormally large resistivity of $Ca_4Mn_3O_{10}$, the doped $Ca_4Mn_{3-x}V_xO_{10}$ system in ref 14, which is similar to the present $Ca_4Mn_{3-x}Nb_xO_{10}$ system, did not exhibit significant variations in resistivity. These phenomena may have also been correlated with the relatively small dopant concentrations in these two systems, as a consequence of which the carrier concentration was too small to lead to large variations in resistivity. Further investigations of this behavior are still in progress.

To further investigate the transport mechanism, attempts to fit the resistivity data to various empirical equations were made. It was found that the high-temperature behavior of all of the samples could be well-described by the small polaron conduction (SPC) model:[34]

$$\rho = \rho_0 T \exp(E_\rho / k_B T)$$

where ρ_0 is a constant and E_ρ represents the activation energy of a small polaron. The fitting results are plotted in Figure 8a, and the E_ρ values obtained from the fits are listed in Table 2. It is clear that E_ρ reached a minimum value of 71.4 meV for the $x = 0.1$ sample and then rose to 74.8 meV for the $x = 0.2$ sample. This result demonstrated that the DE interaction, which can reinforce the itinerancy of the carriers,

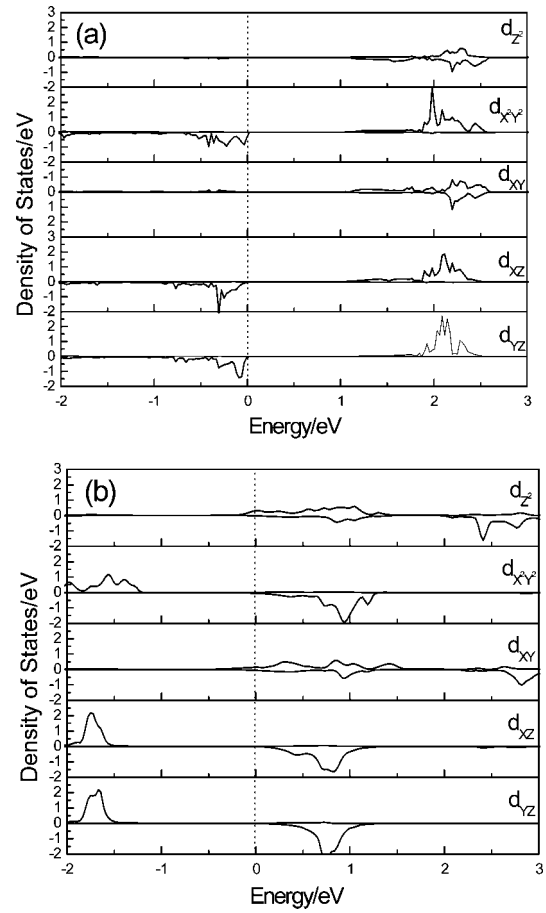

Figure 10. Partial density of states of Mn d orbitals in (a) $Ca_4Mn_3O_{10}$ and (b) $Ca_4Mn_{2.8}Nb_{0.2}O_{10}$.

dominated at low doping levels, leading to a lower activation energy, whereas at high doping levels, local Jahn−Teller distortion and the activity of the dopant atoms as scattering centers became dominant, causing the carriers to be more localized and consequently enhancing the activation energy. On the other hand, it can be seen that at low temperatures, the fitted SPC curves did not agree with the experimental data, indicating some transitions upon cooling. Actually, the low-temperature behaviors were well-fitted by the 2D version of Mott's variable range hopping (VRH) model:[34]

$$\rho = \rho_0 \exp[(T_0/T)^{1/3}]$$

where T_0 is a characteristic temperature associated with $N(E_F)$, the density of states in the vicinity of the Fermi energy, and ζ, the localization length, i.e., $T_0 = 16/k_B N(E_F)\zeta^2$. The fitting results are presented in Figure 8b, and the values of T_0 are listed in Table 2. The values of T_0 for the $x = 0.05$ and $x = 0.1$ samples decreased compared with the value for undoped sample, implying that the density of states in the vicinity of the Fermi surface increased (assuming the variation of the localization length of the carrier to be negligible). However, the T_0 value increased for the $x = 0.2$ sample, indicating strengthened localization of the carrier as a result of partial destruction of the conduction path by the increase in the number of $4d^0$ Nb^{5+} ions.

Magnetoresistance effects were investigated for all of the samples. Figure 9a illustrates the temperature variation of the negative of the magnetoresistance at $H = 5$ T for the

(33) Masunaga, S. H.; Jardim, R. F. *J. Appl. Phys.* **2007**, *102*, 73903.
(34) Mott, N. F.; Davis, E. A. *Electronic Process in Non-Crystalline Materials*; Clarendon: Oxford, U.K., 1979.

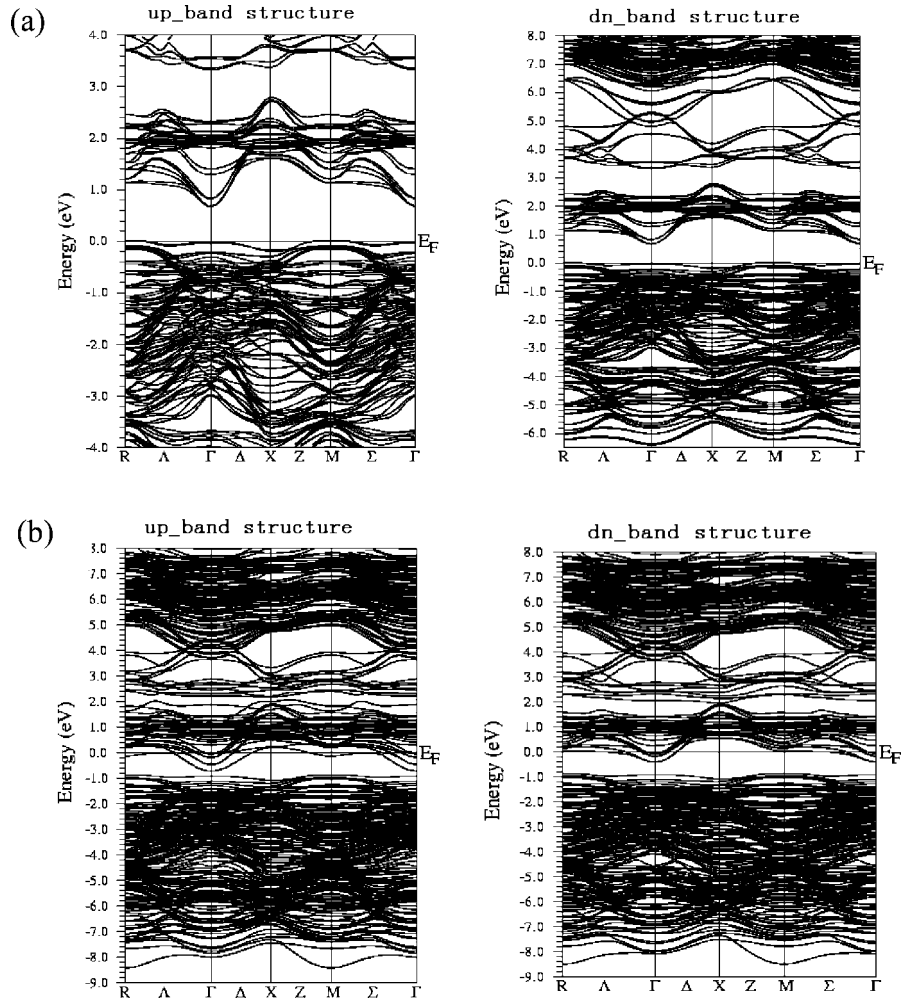

Figure 11. Spin-dependent band structures of (a) $Ca_4Mn_3O_{10}$ and (b) $Ca_4Mn_{2.8}Nb_{0.2}O_{10}$ in the antiferromagnetic states. The line at 0 eV refers to the Fermi energy level.

doped samples; the magnetoresistance is defined as MR = $\{[\rho(H) - \rho(0)]/\rho(0)\} \times 100\%$, where $\rho(H)$ denotes the resistivity at an applied magnetic field H. Clearly, the CMR effect occurred in the low-temperature region below 100 K, and its magnitude increased with decreasing temperature. As the amount of Nb increased, the value of −MR showed a gradual increase and reached a maximum of 51% for $x = 0.2$ at 40 K within our measurement range. Moreover, it is worth mentioning that the CMR effect for the doped samples was significantly larger than that of $Ca_4Mn_3O_{10}$ (not shown), which agreed with the results for the $Ca_4Mn_{3-x}Mo_xO_{10}$ system,[16] reflecting the similarity of the electronic ground states of these systems. The existence of FM clusters was responsible for the CMR behavior because an applied magnetic field can make the randomly oriented FM clusters become a parallel array, facilitating spin-dependent transport and thereby diminishing the resistivity. The enhanced CMR with increased doping was associated with the increase in the number of FM clusters. Figure 9b illustrates the magnetic field dependence of −MR over the range $H = 0-5$ T at 35 K for all of the samples. It is evident that the value of −MR for each sample showed an approximately linear rise as the magnetic field increased, similar to that found for the $Ca_4Mn_{3-x}V_xO_{10}$ system.[14] This feature was reasonable because V and Nb belong to the same group in the periodic table of the elements and thus should possess similar properties. Nevertheless, there were also some differences in the magnitudes of the MR for these two systems. The present −MR values, which reached 59% for the $x = 0.2$ sample under a field of 5 T at 35 K, were greater than those of the $Ca_4Mn_{3-x}V_xO_{10}$ system under the same conditions. We speculate that the greater MR was due to the fact that the ionic radius of Nb^{5+} is larger than that of V^{5+}. The larger Nb^{5+} led to a longer distance between neighboring ions and thus a weaker exchange interaction, which decreased the effective transfer interaction in the charge carriers and consequently caused an increase in the MR magnitude via enhanced effective coupling between the local spin and the charge carriers.[35] The MR observed in the present samples may have had as many as three origins: spin-dependent scattering and spin-polarized interplane and intergrain tunneling. Spin-dependent scattering MR originates from the reduction of spin disorder in the grains by the applied magnetic field. Interplane tunneling MR is related to the layered nature of $Ca_4Mn_{3-x}Nb_xO_{10}$, and intergrain tunneling MR is dependent on the physical grain boundaries. Further synthesis of single-crystal samples is necessary in order to distinguish among these mechanisms in our samples.

(35) Asano, H.; Hayakawa, J.; Masui, M. *Appl. Phys. Lett.* **1997**, *71*, 844.

Calculations on $Ca_4Mn_3O_{10}$ and $Ca_4Mn_{2.8}Nb_{0.2}O_{10}$ were done in order to further confirm our experimental results. To investigate the electron-doping effect of substituting Mn by Nb, we comparatively analyzed the partial density of states of the Mn d orbitals in the two samples (for $Ca_4Mn_{2.8}Nb_{0.2}O_{10}$, Mn^{3+} near the Nb was selected), as shown in Figure 10. Obviously, the Mn d orbitals were indeed injected with electrons in $Ca_4Mn_{2.8}Nb_{0.2}O_{10}$, consistent with our experimental determinations. In addition, compared with those of Mn d orbitals in $Ca_4Mn_3O_{10}$, the energies of both the occupied and unoccupied d orbitals in $Ca_4Mn_{2.8}Nb_{0.2}O_{10}$ were lowered, and the density of states of O p orbitals (not shown) was positioned between −1.5 and −4.0 eV, indicating enhanced hybridization between Mn and O in the Nb-doped compound. The GGA-calculated electronic band structures are shown in Figure 11. For $Ca_4Mn_3O_{10}$, both the spin-up and spin-down bands showed semiconductor character, while for $Ca_4Mn_{2.8}Nb_{0.2}O_{10}$, the bands around the Fermi level were partially filled. As previous work[36] has pointed out, it is important to recall that a system with partially filled bands can be a normal metal but is also subject to electron localization induced by electron–electron repulsion (Mott−Hubbard localization), by random potentials associated with lattice defects (Anderson localization), or by electron–phonon coupling as found for polaron states. Electron localization causes the extent of the electron wave function to have a finite length ζ. If this localization length ζ is small, the electrons are strongly localized, and the system behaves as an insulator: its charge transport occurs through hopping, and its resistivity increases strongly with decreasing temperature. In the present work, the resistivity behavior at low temperature was well-fitted by the 2D version of Mott's VRH model with a relatively high density of states at the Fermi level. Therefore, the electronic band structure of $Ca_4Mn_{2.8}Nb_{0.2}O_{10}$ obtained from the GGA calculations, which showed partially filled bands, was consistent with the experimental results.

(36) Gourdon, O.; Evain, M.; Jobic, S.; Brec, R.; Koo, H. J.; Whangbo, M. H. *Inorg. Chem.* **2001**, *40*, 2898.

Conclusions

A series of compounds having the Ruddlesden–Popper structure, $Ca_4Mn_{3-x}Nb_xO_{10}$ ($x = 0$–0.2), have been investigated. The orthorhombic crystal structures with space group *Pbca* were established by powder XRD refinement. Increases in both unit cell volume and divergence among Mn−O bond lengths upon Nb doping were consistent with an increase in the amount of the Mn^{3+} Jahn–Teller ion. Nb doping in $Ca_4Mn_3O_{10}$ led to injected electrons in Mn sites, as confirmed by both the experimental results and theoretical calculations, and thus ferromagnetic clusters appeared through double exchange between Mn^{3+} and Mn^{4+}. All of the samples exhibited semiconducting behavior over the whole measured temperature range; this behavior at high temperature followed the small polaron conduction model, whereas the low-temperature behavior obeyed the 2D version of Mott's variable range hopping model, which agreed well with the results of the GGA calculations. A significant magnetoresistance effect was observed for the doped samples in comparison with the undoped sample. The measured magnetic field dependence of the MR revealed that the MR effect in the present $Ca_4Mn_{3-x}Nb_xO_{10}$ compounds was larger than that in the analogous $Ca_4Mn_{3-x}V_xO_{10}$ system.

Acknowledgment. We gratefully acknowledge financial support (Grants 20331030, 20671088, 20601026, and 20771100) from the National Natural Science Foundation of China (NSFC).

CM071712S